EF-3DGS: Event-Aided Free-Trajectory 3D Gaussian Splatting

Bohao Liao, Wei Zhai, Zengyu Wan, Tianzhu Zhang, Yang Cao and Zheng-Jun Zha, *Member, IEEE*

Abstract—Scene reconstruction from casually captured videos has wide applications in real-world scenarios. With recent advancements in differentiable rendering techniques, several methods have attempted to simultaneously optimize scene representations (NeRF or 3DGS) and camera poses. Despite recent progress, existing methods relying on traditional camera input tend to fail in high-speed (or equivalently low-frame-rate) scenarios due to insufficient observations and large pixel displacements between adjacent frames. Event cameras, inspired by biological vision, record pixel-wise intensity changes asynchronously with high temporal resolution and low latency, providing valuable scene and motion information in blind inter-frame intervals. In this paper, we introduce the event camera to aid scene construction from a casually captured video for the first time, and propose Event-Aided Free-Trajectory 3DGS, called EF-3DGS, which seamlessly integrates the advantages of event cameras into 3DGS through three key components. First, we leverage the Event Generation Model (EGM) to fuse events and frames, supervising the rendered views observed by the event stream. Second, we adopt the Contrast Maximization (CMax) framework in a piece-wise manner to extract motion information by maximizing the contrast of the Image of Warped Events (IWE), thereby calibrating the estimated poses. Besides, based on the Linear Event Generation Model (LEGM), the brightness information encoded in the IWE is also utilized to constrain the 3DGS in the gradient domain. Third, to mitigate the absence of color information of events, we introduce photometric bundle adjustment (PBA) to ensure view consistency across events and frames. Additionally, we propose a Fixed-GS training strategy that separates the optimization of scene structure and color, effectively addressing color distortions caused by the lack of color information in events. We evaluate our method on the public Tanks and Temples benchmark and a newly collected real-world dataset, RealEv-DAVIS. Our method achieves up to 2dB higher PSNR and 40% lower Absolute Trajectory Error (ATE) compared to state-of-the-art methods under challenging high-speed scenarios. Our project page is https://lbh666.github.io/ef-3dgs/.

Index Terms—Event Camera, Novel View Synthesis, 3D Gaussian Splatting, Neural Rendering

I. INTRODUCTION

IN recent years, Neural Radiance Fields (NeRF) [1]–[3] and 3D Gaussian splatting (3DGS) [4], [5] have made significant progress in novel view synthesis tasks. Given a set of posed images of the same scene, they optimize an implicit or explicit scene representation using volume rendering. While subsequent methods [2], [3], [6], [7] have made great strides in rendering quality and speed, how to reconstruct the scene from a video captured with free camera trajectories remains

Bohao Liao, Wei Zhai, Zengyu Wan, Tianzhu Zhang, Yang Cao and Zheng-Jun Zha are at the University of Science and Technology of China, Anhui, China. (e-mail: {liaobh, wanzengy}@mail.ustc.edu.cn, {wzhai056, tzzhang, forrest, zhazj}@ustc.edu.cn)

an open problem. It has great application potential in the real world, such as in VR/AR, video stabilization, and mapping. To tackle this challenging task, several efforts have been made.

Free-trajectory videos often cover a vast field of view, so a key challenge is how to preserve the detailed textures of the foreground while representing the overall large-scale scene. Previous methods [8], [9] adopt different spatial transformation and allocation approaches based on neighboring frames' viewing angles and range to achieve efficient and high-quality scene reconstruction. Another challenge is that accurate pose estimation is often difficult to obtain in free-trajectory scenarios. Previous methods [9], [10] have incorporated priors, such as the depth [11]–[13] and the optical flow [14], into their loss functions to improve pose estimation or modify their optimization strategies. While these methods above can render photo-realistic images in typical free-trajectory scenarios, the rendering quality degrades significantly in high-speed scenarios (or equivalent low-frame-rate scenarios). This type of scenario has essential applications in the real world, such as autonomous driving or FPV exploration. Besides, the significant motion between consecutive frames poses challenges for feature matching and further abrupt pose estimation (as shown in the third row of Fig.1). This makes it even more crucial for the algorithm to robustly estimate the poses in such scenarios.

The performance degradation of prior methods can be attributed to two primary factors. Firstly, the limited number of camera observations leads to an under-constrained scene reconstruction problem. This can cause the scene representation to converge to a trivial solution [15]–[17], where the model overfits to the training views without capturing the correct underlying geometry structure. Consequently, the synthesized images from novel viewpoints exhibit visual artifacts. Secondly, the substantial discrepancies between consecutive frames, resulting in diminished overlapping regions, violate the implicit assumption of continuous motion between adjacent frames, which was leveraged by previous techniques such as LocalRF [9] and NoPe-NeRF [10]. This significant violation greatly exacerbates the ill-posedness of the joint optimization of scene and camera poses, further deteriorating the quality of the synthesized novel views.

Event camera is a bio-inspired image sensor that asynchronously records per-pixel brightness changes, offering advantages such as high temporal resolution, high dynamic range, and no motion blur [18]–[23]. The brightness information recorded in the event stream can effectively complement the missing scene information between consecutive frames. Moreover, in scenarios with stable scene illumination, the event data naturally encodes the motion information of the
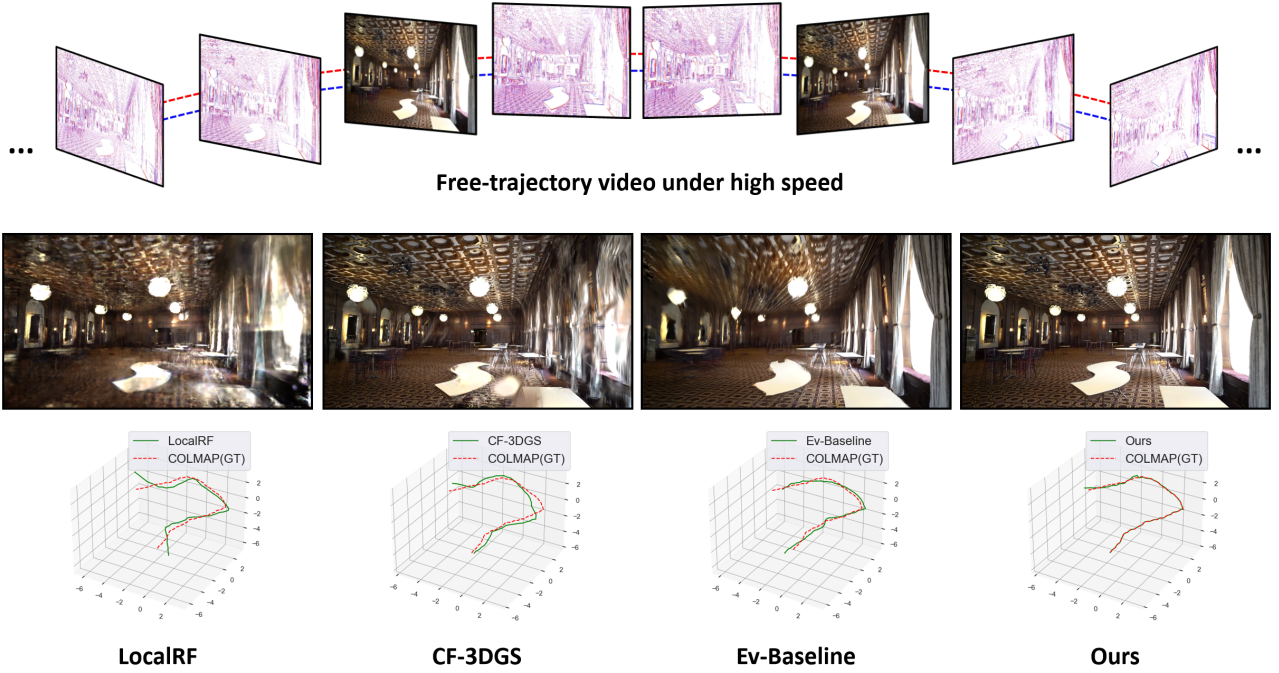
Fig. 1: Free-trajectory 3DGS under high speed. The top row shows the overall paradigm. The colored dots (red for positive and blue for negative events) in the top row represent the event data. Given free-trajectory video and corresponding event stream under the high-speed scenario, we aim to jointly estimate poses and the 3DGS. Our method surpasses current state-of-the-art methods in terms of both rendered results (middle row) and pose estimation (bottom row).

scene [24]–[26], containing rich motion cues. These properties make event cameras well-suited for scene reconstruction tasks in high-speed and free-trajectory scenarios [27]. However, seamlessly integrating the aforementioned benefits of event cameras is nontrivial. First, NeRF or 3DGS renders absolute pixel brightness, which aligns with image data. In contrast, event stream records sparse scene brightness changes, lacking the ability to perceive absolute brightness, and most event cameras lack color information. Second, the motion cues in event cameras is encoded in the spatio-temporal correlations of the event stream. In contrast, previous methods typically sample and optimize frames and pixels independently, without explicitly considering these temporal correlations.

In this work, we propose Event-Aided Free-Trajectory 3DGS, dubbed EF-3DGS, a framework that integrates event data into the scene optimization process to fully leverage the high temporal resolution property of event cameras. Specifically, based on the Event Generation Model (GEM), we introduce an event-based re-render loss, which extends the 3DGS optimization to the continuous event stream. This allows us to effectively utilize the brightness cues encoded in the event streams between adjacent frames, providing rich supervisory signals to alleviate the problem of insufficient sparse viewpoints. Regarding the pose estimation challenge, we introduce the CMax [28] framework to exploit the spatio-temporal correlations of events. We obtain the motion field by leveraging the pseudo-depth from 3DGS rendering and the relative camera motion between consecutive time. We then warp the events triggered by the same edge along the motion trajectories to maximize the sharpness of the image of warped events

(IWE), thereby estimating the motion that best matches the current spatio-temporal event patterns. Furthermore, through the Linear Event Generation Model (LEGM) [29], [30], we establish a connection between motion and brightness changes. This allows us to constrain the 3DGS in the gradient domain using the IWE. Finally, as event data primarily records scene brightness changes, lacking color information, we introduce photometric bundle adjustment (PBA) and a Fixed-GS strategy to address this. PBA recovers color by optimizing reprojection errors onto RGB frames, while Fixed-GS enables separate optimization of scene structure and color.

Our main contributions are summarized as follows:

- We introduce event cameras into the task of free-trajectory scene reconstruction for the first time. Its advantage of high temporal resolution and low latency showcases the potential of event data for scene reconstruction tasks in challenging scenarios.
- We derive our method from the underlying imaging principles of event cameras and design the corresponding loss functions that mine the motion and brightness information encoded in event data and seamlessly integrate them into the 3DGS optimization.
- Experiments on both public benchmarks and real-world datasets demonstrate that our method significantly outperforms existing state-of-the-art approaches in terms of both rendering quality and trajectory estimation accuracy. Our method achieves up to 2dB higher PSNR and 40% lower Absolute Trajectory Error compared to state-of-the-art methods in high-speed scenarios.

II. RELATED WORKS

A. *Large Scale Scene Reconstruction*

The reconstruction of large scenes has emerged as a significant area of research over the past decade. Traditional approaches [31], [32] rely on Structure from Motion techniques to recover camera poses and sparse 3D point clouds. The introduction of NeRF [1] marked a paradigm shift in scene representation and reconstruction. Several works [2], [33], [34] have attempted to extend NeRF to unbounded scenes. F2-NeRF [8] adopts perspective warping based on the local viewing range to handle free-viewpoint unbounded scenes. To extend unbounded scenes to large-scale scenes, Mega-NeRF [35] and Block-NeRF [36] adopt a divide-and-conquer strategy. LocalRF [9] allocates new radiance fields dynamically according to the distance between the current view and the previous radiance field. Recently, 3D Gaussian Splatting (3DGS) has been extended to large-scale scene reconstruction due to its efficient rendering capabilities and explicit 3D representation. CityGaussian [37] and VastGaussian [38] adopt spatial allocation strategies similar to Mega-NeRF [35]. CityGaussian [37] dynamically selects poses for optimization based on visibility criteria, while VastGaussian [38] employs a visibility-driven progressive approach to dynamically select both training poses and Gaussian points for optimization. In contrast to these methods, which primarily focus on scalability and often require precomputed camera poses from COLMAP [39], we focus on the challenges of reconstructing scene from casually captured free-trajectory videos without relying on precomputed poses.

B. *Joint Pose and Scene Optimization*

The research community has recently focused on developing methods [5], [9], [10], [17], [40]–[42] that can be optimized without requiring precomputed camera poses. A line of work has focused on improving the stability of the optimization process. GARF [41] and BARF [42] both find that the high-frequency position encoding is prone to local minima and try to improve it. For example, GARF [41] proposes using Gaussian activation to replace the sinusoidal position encoding. Another line of work has investigated incorporating additional constraints to make the problem more tractable. SPARF [17] incorporates cross-view feature matching constraints and depth consistency regularization. More recent approaches [5], [9], [10] leverage pre-trained networks, *i.e.*, monocular depth estimation and optical flow estimation, to obtain additional priors and better address the pose-free NeRF reconstruction problem. Exploiting 3DGS's explicit representation, CF-3DGS [5] directly back-projects Gaussian points using depth maps, enhancing the utilization of depth priors. While the aforementioned methods have made notable progress, they have yet to fully address the challenges posed by high-speed (or equivalently sparse-view) scenarios or rely on a good pose initialization. Our approach addresses these issues by leveraging motion and brightness cues from event streams.

C. *Event-Based Novel view Synthesis*

Recent works have explored the integration of event cameras into the NeRF framework. Early approaches, such as E-NeRF [43] and EventNeRF [44], utilize event-based generative models, minimizing the difference between the rendered brightness changes and observed brightness changes calculated by the accumulated events. Building upon this, Robust e-NeRF [45] incorporates a more realistic imaging model into the event-based framework, accounting for factors like refractory periods and noise. Beyond event-based NeRF, efforts have also been made to integrate event data into image-based methods. For instance, E2NeRF [46] and EvDeblurNeRF [47] leverage the Event Double Integral (EDI) [48] model to address the deblurring problem, while DE-NeRF [49] and EvDNeRF [50] leverage the high temporal resolution property of event camera to capture fast-moving elements in dynamic scene. A key distinction of our work is that, unlike the prior methods that rely on accurate precomputed poses, we jointly optimize for both the camera poses and the scene representation. Furthermore, while previous works have been limited to simulated environments or simple indoor scenes, we evaluate our approach in large-scale outdoor scenarios.

III. PRELIMINARY

3DGS [4] parametrizes the 3D scene as a set of 3D gaussians $\{G_k\}_{k=1}^K$ that carry the geometric and appearance information. Each 3D Gaussian is characterized by several learnable properties, including its center position $\mu \in \mathbb{R}^3$, opacity $\alpha \in [0, 1]$, spherical harmonics (SH) features $\mathbf{f}_k \in \mathbb{R}^{3 \times 16}$ for view-dependent color $c \in \mathbb{R}^3$, rotation matrix $R \in \mathbb{R}^{3 \times 3}$ (stored in quaternion form), scale factor $s \in \mathbb{R}^3$. The shape of each Gaussian is defined by the covariance matrix $\mathbf{\Sigma}$ and the center (mean) point μ,

$$G(x) = \exp(-\frac{1}{2}(x - \mu)^T \mathbf{\Sigma}^{-1}(x - \mu)). \tag{1}$$

To preserve the valid positive semi-definite property during optimization, the $\mathbf{\Sigma}$ is derived by the scale factor s and the rotation factor R,

$$\mathbf{\Sigma} = RSS^T R^T. \tag{2}$$

Before rendering, the Gaussian is first projected to the 2D image plane:

$$\mathbf{\Sigma}^{2D} = JW\mathbf{\Sigma}W^T J^T, \tag{3}$$

where J is the Jacobian of the affine approximation of the projective transformation, and W is the viewing transformation. During rendering, a tile-based rasterizer is applied to enable fast sorting and α-blending. The color of each pixel is calculated via blending N ordered overlapping points:

$$C(\mathbf{r}) = \sum_{i=1}^{N} c_i \alpha_i \prod_{j=1}^{i-1}(1 - \alpha_j), \tag{4}$$

where c_i is calculated from spherical harmonics and view direction, α_i is the multiplication of opacity and the transformed 2D Gaussian and $\mathbf{r}$ denotes the image pixel. With the forward
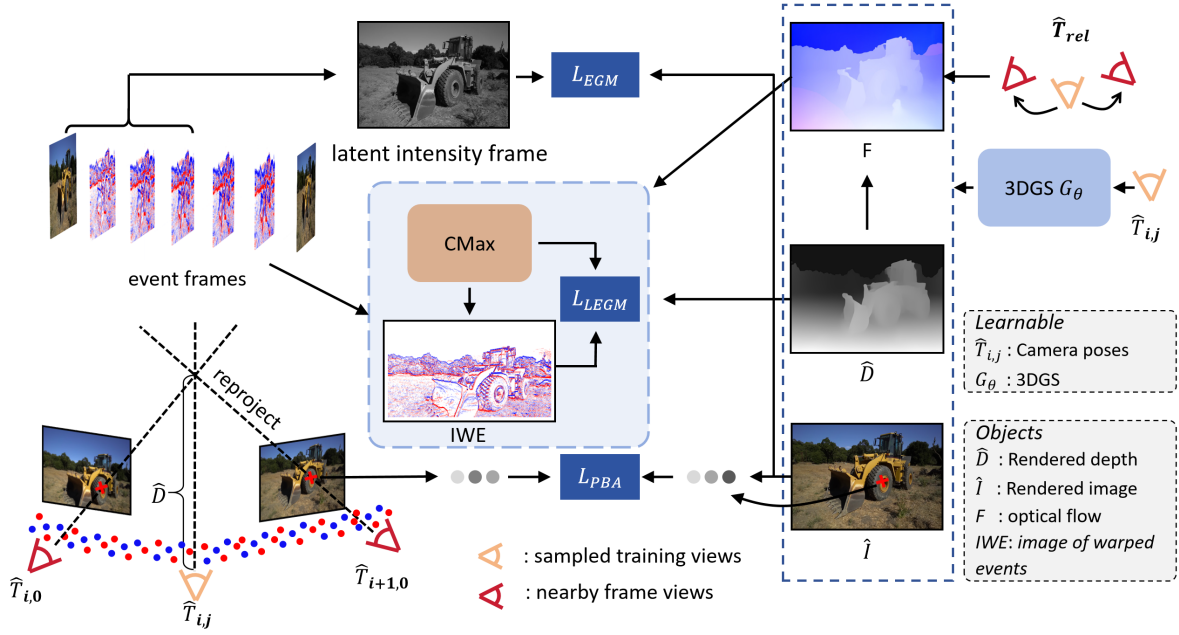
Fig. 2: Method Overview. Our method takes video frames $\{I_i\}$ and event stream $\varepsilon = \{\mathbf{e}_k\}$ as input. During training, we random sample $t \in \{t_{i,j}\}$, leveraging the events within current subinterval and most recent frame to establish the proposed three main constrains,$\mathcal{L}_{EGM}$, $\mathcal{L}_{LEGM}$ and $\mathcal{L}_{PBA}$. The colored dots (red for positive and blue for negative events) represent the event data. The details of $\mathcal{L}_{LEGM}$ and CMax framework are illustrated in Fig. 3

rendering procedure, we can optimize 3DGS by minimizing the photometric loss between observation and rendered pixels:

$$\mathcal{L}_{color} = (1-\lambda)\mathcal{L}_1(\hat{I}, I) + \lambda\mathcal{L}_{D-SSIM}(\hat{I}, I), \quad (5)$$

where the first term is a standard $\mathcal{L}_1$ loss between the target and rendered images, $\mathcal{L}_{D-SSIM}$ is a differentiable version of structural similarity index and λ is balancing weight which is set to 0.2 following [4]. As this optimization is highly sensitive to local minima, 3DGS additionally employs periodic adaptive densification and pruning of splats. By integrating depth t_i of each Gaussian in Equation (4) along the ray, we can also obtain a expected depth value $\hat{D}(\mathbf{r})$:

$$\hat{D}(\mathbf{r}) = \sum_{i=1}^{N} t_i \alpha_i \prod_{j=1}^{i-1}(1-\alpha_j). \quad (6)$$

IV. METHOD

In this section, we introduce our method. The overall framework is shown in Fig. 2. Given a video of a free-trajectory $\{I_i\}$ captured at time $\{t_i\}$ and an event stream $\varepsilon = \{\mathbf{e}_k\}$, our goal is to reconstruct the 3DGS of the scene and the corresponding camera trajectory$\{T_i\}$. The photometric loss of the original 3DGS follows an analysis-by-synthesis process. Similarly, in order to incorporate the events into the 3DGS optimization process, we delve into the imaging principles of event cameras. Revolving around the Event Generative Model (**EGM**) and Linearized Event Generative Model (**LEGM**), we establish constraints from the connection between motion and brightness changes. Further, through photometric bundle adjustment (**PBA**) and **Fix-GS** training strategy, we mitigate the absence of color information of events and further strengthen the consistency of cross-view rendering.

A. EGM Driven Optimization

The Event Generation Model (EGM) describes the base working principle of event cameras, which capture pixel-wise brightness changes asynchronously. When the logarithmic brightness change at a pixel $\mathbf{u}_k = (x_k, y_k)$, exceeds a predefined contrast threshold C,

$$\Delta L(\mathbf{u}_k, t_k) \doteq L(\mathbf{u}_k, t_k) - L(\mathbf{u}_k, t_k - \delta t) = p_k C, \quad (7)$$

where $L \doteq log(I)$ is the logarithm of intensity, $p_k \in \{-1, +1\}$ indicates the polarity of brightness changes, and t_k is the triggered timestamp. By leveraging the high temporal resolution of event cameras, we can effectively constrain the 3DGS optimization process in the temporal domain.

To incorporate the event data into the optimization process, we first divide the time interval between two adjacent video frames I_i and I_{i+1} into N smaller subintervals $\varepsilon_{i,j} = \{\mathbf{e}_k | t_{i,j} \le t_k \le t_{i,j+1}, \Delta t = \frac{t_{i+1}-t_i}{N}, t_{i,j} = t_i + j \cdot \Delta t\}$. This allows us to form event frames at a higher temporal resolution than the original video frames:

$$E_{i,j} = \sum_{e_k \in \varepsilon_{i,j}} p_k. \quad (8)$$

We then reconstruct the latent intensity image I_t at any intermediate time $t \in \{t_{i,j}\}$ between two video frames I_i and I_{i+1} using the accumulated events and the most recent frame:

$$I_t = I_{i,j} = \begin{cases} I_{i,0} \cdot \exp(\sum_{n=0}^{j-1} E_{i,n} \cdot C) & \text{if } j > 0 \\ I_{i,0} & \text{if } j = 0 \end{cases}. \quad (9)$$

Then, the event-based rendering loss is introduced to enforce the consistency between rendered and latent intensity images:

$$\mathcal{L}_{EGM} = (1-\lambda)\mathcal{L}_1(\hat{I}_t, I_t) + \lambda\mathcal{L}_{D-SSIM}(\hat{I}_t, I_t). \quad (10)$$

This loss function ensures that the 3DGS optimization process is constrained not only by the sparse video frames but also by the dense event data, leading to improved reconstruction quality. It is worth noting that when $j = 0$, the latent intensity image I_t is equal to the first most recent video frame $I_{i,0}$ and $\mathcal{L}_{EGM}$ reduces to the standard image rendering loss.

B. Unified CMax and LEGM Optimization

While $\mathcal{L}_{EGM}$ leverages the brightness change information recorded by the events, it does not explicitly exploit the motion information encoded in the event stream. To further improve the accuracy of camera poses and the reconstructed 3DGS, we introduce the Contrast Maximization (CMax) [28], [51], [52] framework and the Linear Event Generation Model (LEGM) [29], [30], [53] in this section. These models complement the EGM-driven optimization by extracting motion cues and gradient information from the event stream, providing additional constraints for the 3DGS optimization process.

Under the assumption of constant scene illumination, events are triggered solely by the motion of scene edges. The edges in the scene form continuous trajectories in the (x, y, t) space. Intuitively, by back-projecting the events along the correct motion trajectories, we can obtain a sharp image of warped events (IWE). Therefore, the sharpness of the IWE can serve as an indication of the accuracy of the currently estimated motion. This insight motivates us to derive a motion field by leveraging the rendered depth from 3DGS using eq. (6) and the relative camera motion between neighboring timestamps. By optimizing the sharpness of the IWE, we can obtain the optimal motion field, which in turn helps to improve the geometric accuracy of the 3DGS and the relative poses between adjacent frames.

Instead of warping each event as in the original CMax framework, we adopt a piece-wise warping approach for efficiency. Specifically, we first accumulate the events within each sub-interval to obtain event frames $E_{i,j}$ as in eq. (8) . Then, for randomly sampled timestamps $t_{ref} = t_{i,j}$, we warp the event frames in the neighboring $2r$ sub-intervals to t_{ref}:

$$E_{i,j-m \to j} = \text{warp}(E_{i,j-m}, F_{i,j \to j-m}), \quad (11)$$

where $m \in [-r, r]$, $F_{i,j-m \to j}$ is the optical flow which can be derived from the rendered depth $\hat{D}$ in eq. (6) and relative pose $T_{i,j \to j-m}$ between two timestamps:

$$F_{i,j \to j-m} = \Pi(T_{i,j \to j-m}\Pi^{-1}(x, y, \hat{D})) - (x, y), \quad (12)$$

where $T_{i,j \to j-m} = T_{i,j-m}T_{i,j}^{-1}$, Π projects a 3D point to image coordinates and Π^{-1} unprojects a pixel coordinate and depth into a 3D point. Then the image of piece-wise warped events (IPWE) at timestamp $t_{i,j}$ is computed by averaging the warped event frames:

$$\text{IPWE}_{i,j} = \frac{1}{2r+1} \sum_{m=j-r}^{j+r} E_{i,m \to j} \approx \frac{1}{C}\Delta L. \quad (13)$$

Following the Cmax framework, we maximize the variance of the IPWE, which is equivalent to minimize its opposite:

$$\mathcal{L}_{cm} = -\text{Var}(\text{IPWE}_{i,j}). \quad (14)$$

Maximizing the contrast encourages the motion field to align with the actual motion of edges, leading to sharper IPWEs. This objective helps to improve the accuracy of the estimated camera poses and the geometric consistency of the 3DGS reconstruction. Furthermore, based on the Linear Event Generation Model (LEGM) [29], [30], the brightness change ΔL at pixel $\mathbf{u}$ can be approximated by the dot product of the image gradient ∇L and the optical flow $\dot{\mathbf{u}}$ (note that L is the logarithm of a image):

$$\Delta L(\mathbf{u}) = -\nabla L \cdot \dot{\mathbf{u}} \approx L(\mathbf{u}) - L(\mathbf{u} + \dot{\mathbf{u}}). \quad (15)$$

It is noteworthy that the IPWE also encodes brightness change information. Combining eq. (13) and eq. (15), we establish a connection between the IPWE and the brightness changes of the rendered images:

$$C \cdot \text{IPWE}_{i,j} = \hat{L}(\mathbf{u}) - \hat{L}(u + F_{i,j \to j+1}). \quad (16)$$

Based on this relationship, we formulate an additional gradient-based loss to constrain the 3DGS optimization:

$$\mathcal{L}_{grad} = ||C \cdot \text{IPWE}_{i,j} - (\hat{L}(\mathbf{u}) - \hat{L}(u + F_{i,j \to j+1}))||^2, \quad (17)$$

where $\hat{L}$ is the logarithm of synthesised image $\hat{I}_t$. Finally, the full LEGM loss is defined as:

$$\mathcal{L}_{LEGM} = \lambda_{cm}\mathcal{L}_{cm} + \lambda_{grad}\mathcal{L}_{grad}, \quad (18)$$

where λ_{cm} and λ_{grad} are the balancing weight coefficients for $\mathcal{L}_{cm}$ and $\mathcal{L}_{grad}$ respectively.

C. Photometric Bundle Adjustment

The aforementioned event-based constrains, $\mathcal{L}_{EGM}$ and $\mathcal{L}_{LEGM}$, leverage the brightness change and motion information encoded in the event data to constrain 3DGS. However, as event cameras only record brightness changes and lack color perception, directly applying them to 3DGS optimization may lead to inconsistent color rendering. To ensure cross-view consistency of the 3DGS rendering, we introduce the Photometric Bundle Adjustment (PBA) term.

Specifically, for a randomly sampled timestamp $t \in \{t_{i,j}\}$, we establish the following photometric reprojection error:

$$\mathcal{L}_{PBA} = \sum_{\mathbf{u} \in \mathcal{P}} \sum_{I_s \in \mathcal{F}} ||I_s(\mathbf{u}') - \hat{I}(\mathbf{u})||^2, \quad (19)$$

where $\mathbf{u}' = \Pi(T_{i,j-r \to j}\Pi^{-1}(x, y, \hat{D}(u)))$ represent the coordinate on target view projected from the pixel $\mathbf{u}$ of source view I_s, $\mathcal{P}$ denotes the pixel samples of current frame, and $\mathcal{F}$ is the candidates of target video frames. We select $\mathcal{F}$ to be the adjacent video frames in consideration of computation costs.

By minimizing $\mathcal{L}_{PBA}$ over sampled pixels in the event frames and neighboring video frames, we encourage the 3DGS model to produce geometrically and photometrically consistent renderings across events and video frames.
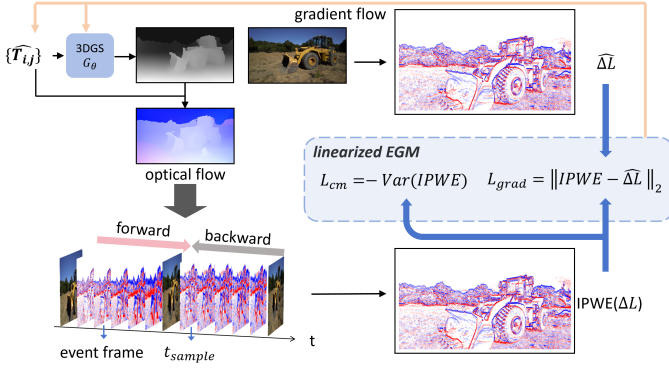
Fig. 3: The illustration of unified CMax and LEGM optimization. We warp nearby event frames to the sampled timestamp through the optical flow and maximize the sharpness of the image of piece-wise warped events (IPWE). The byproduct IWPE is utilized to establish additional constrain on 3DGS in gradient domain.

D. Fixed-GS Training Strategy

As demonstrated in Fig. 10, the $\mathcal{L}_{PBA}$ term alone is insufficient to fully mitigate color distortion issues. The absence of color information in event data poses a significant challenge for scene reconstruction in previous NeRF-based methods. NeRF models employ implicit representations [54], utilizing MLPs to store scene color and density information in a coupled manner. Consequently, color distortions can affect scene density estimations and vice versa. In contrast, 3DGS explicitly stores various attributes independently within Gaussian points. This characteristic allows us to address color distortion issues specifically while maintaining other attributes.

To leverage this advantage, we propose a two-stage **Fixed-GS** scene optimization strategy. In the first stage, optimization is performed across all timestamps:

$$G_\theta^* = \underset{\alpha,r,s,f}{\arg\min} \ \mathcal{L}_{event}, \ t \in \{t_{i,j}\}, \qquad (20)$$

where α, r, s, f is the opacity, rotation, scale factor and spherical harmonics of Gaussians, and t is the sampled timestamp during training. This stage results in a scene reconstruction with accurate structure and brightness, albeit with potential color distortions. The second stage focuses on recovering accurate color information. During this phase, optimization is conducted exclusively on video frames. Capitalizing on the explicit representation of Gaussians, we optimize only the spherical harmonic coefficients of the Gaussians while keeping other parameters fixed.

$$G_\theta^* = \underset{f}{\arg\min} \ \mathcal{L}_{event}, \ t \in \{t_{i,0}\} \qquad (21)$$

The ratio between the first and second stages is empirically set to 4:1. This approach allows us to effectively address the color distortion problem while preserving the structural and brightness information obtained from the event data.

E. Overall Training Pipeline

Assembling all loss terms, we get the overall loss function for events:

$$\mathcal{L}_{event} = \mathcal{L}_{EGM} + \mathcal{L}_{LEGM} + \lambda_{PBA}\mathcal{L}_{PBA}, \qquad (22)$$

where λ_{PBA} are the weighting factor. It is noteworthy that since event cameras typically record only the changes in brightness intensity, the $\mathcal{L}_{EGM}$ and $\mathcal{L}_{LEGM}$ losses are computed in the grayscale domain, whereas the $\mathcal{L}_{PBA}$ loss is calculated in RGB color space. We borrow the idea of dynamic scene allocation strategies from LocalRF [9]. Our overall training pipeline builds upon the pipeline of CF-3DGS [5] while introducing novel components to integrate event camera data for free-trajectory scene reconstruction. Further implementation details are provided in the Supplementary Material.

V. EXPERIMENTS

A. Dataset

1) Tanks and Temples: We conduct comprehensive experiments on the Tanks and Temples dataset [55]. Similar to LocalRF [9], we adopt the same 9 scenes, covering large-scale indoor and outdoor scenes. For each scene, we sample a video clip with a 50-second duration, typically featuring free camera trajectories and covering a considerable distance. Following LocalRF [9], we spatially downsample the videos to a resolution of 1080p. Increasing motion speed makes frames further apart, hence it is effectively equivalent to reducing the frame rate. We employ various temporal downsamplings to evaluate the robustness of different methods to varying camera speed scenes. In the 6 FPS setting, we retain one in every five frames as in LocalRF [9]. We perform corresponding frame downsampling for the other frame rate settings (4 FPS, 3 FPS, 2 FPS, and 1 FPS). To synthesize realistic event data, we first upsample the original videos by [56] and then apply the simulator V2E [57].

2) RealEv-DAVIS: Due to the current lack of datasets featuring free-trajectory captures from event cameras, we introduce the RealEv-DAVIS dataset, encompassing four outdoor scenes. We use the DAVIS346 camera, which simultaneously records image frames and events at a resolution of 346x260 pixels. To simulate real-world free-trajectory scenarios, we capture handheld footage at 25 FPS, with each sequence lasting 40 seconds. For SLOW scenarios, we downsample the video clips by keeping every second frame. We further reduce the frame rate in FAST scenarios by retaining only one frame out of every five.

B. Implementation details

Our implementation is primarily based on the PyTorch framework, and we follow the optimization parameters by the configuration outlined in the 3DGS [4] unless otherwise specified. All the parameters are optimized using Adam [58] with $\beta_1 = 0.9$ and $\beta_2 = 0.99$. We optimize the camera poses in the representation of quaternion rotation. The initial learning rate is set to 10^{-5} and gradually decay to 10^{-6} until convergence. The balancing weight λ_{cm}, λ_{grad} and λ_{PBA} is empirically

TABLE I: Quantitative Evaluations on Tanks and Temples. Each baseline method is trained with its public code under the original settings and evaluated with the same evaluation protocol. The best results are highlighted in bold.

Methods	Pose-Free	Input	6 FPS			4 FPS			3 FPS			2 FPS			1 FPS		
			PSNR↑	SSIM↑	LPIPS↓	PSNR↑	SSIM↑	LPIPS↓	PSNR↑	SSIM↑	LPIPS↓	PSNR↑	SSIM↑	LPIPS↓	PSNR↑	SSIM↑	LPIPS↓
F2-NeRF	✗	F	23.55	0.75	0.34	22.97	0.72	0.36	22.25	0.69	0.40	21.64	0.68	0.44	20.63	0.64	0.51
Nope-NeRF	✓	F	13.86	0.51	0.67	13.81	0.51	0.67	13.79	0.51	0.67	13.50	0.51	0.68	13.72	0.51	0.68
LocalRF	✓	F	23.94	0.73	0.36	23.05	0.71	0.39	22.49	0.69	0.40	21.20	0.66	0.44	19.42	0.63	0.48
CF-3DGS	✓	F	26.05	0.78	0.31	25.03	0.77	0.33	23.73	0.74	0.36	22.08	0.68	0.42	20.53	0.65	0.46
EvDeblurNeRF	✗	E+F	22.43	0.71	0.38	21.23	0.69	0.42	20.09	0.65	0.49	17.52	0.62	0.55	15.19	0.55	0.60
ENeRF	✗	E+F	23.62	0.73	0.37	22.84	0.70	0.38	21.85	0.69	0.41	20.52	0.66	0.46	18.09	0.60	0.52
Ev-Baseline	✓	E+F	26.07	0.78	0.32	25.48	0.77	0.33	24.61	0.75	0.36	22.81	0.70	0.38	21.73	0.67	0.43
EF-3DGS(Ours)	✓	E+F	**26.66**	**0.79**	**0.30**	**26.01**	**0.78**	**0.30**	**25.38**	**0.77**	**0.31**	**24.43**	**0.74**	**0.34**	**23.96**	**0.72**	**0.36**

TABLE II: Pose accuracy on Tanks and Temples. Note that we use COLMAP poses in Tanks and Temples as the "ground truth". The unit of RPE_r is in degrees, ATE is in the ground truth scale and RPE_t is scaled by 100. Those methods which require precomputed poses are excluded.

Methods	Input	6 FPS			4 FPS			3 FPS			2 FPS			1 FPS		
		RPE_t↓	RPE_r↓	ATE↓	RPE_t↓	RPE_r↓	ATE↓	RPE_t↓	RPE_r↓	ATE↓	RPE_t↓	RPE_r↓	ATE↓	RPE_t↓	RPE_r↓	ATE↓
Nope-NeRF	F	0.1141	0.7563	2.8382	0.1604	1.0542	2.7653	0.2220	1.3694	2.7857	0.3131	1.8965	2.8412	0.6216	3.913	2.6592
LocalRF	F	0.0806	0.9282	0.5630	0.0867	0.9683	0.6085	0.0911	0.9800	0.6501	0.0957	1.0428	0.6802	0.1421	1.4725	1.0006
CF-3DGS	F	0.0594	0.6981	0.4212	0.0637	0.7128	0.4628	0.0712	0.7531	0.5189	0.0859	0.8074	0.6918	0.1057	0.9768	0.8972
Ev-Baseline	E+F	0.0461	0.5972	0.3419	0.0490	0.6269	0.3766	0.0538	0.6728	0.4261	0.0591	0.7094	0.4860	0.0657	0.7597	0.5534
EF-3DGS(Ours)	E+F	**0.0391**	**0.5427**	**0.2885**	**0.0407**	**0.5521**	**0.3064**	**0.0426**	**0.5796**	**0.3271**	**0.0449**	**0.5953**	**0.3671**	**0.0487**	**0.6259**	**0.3753**

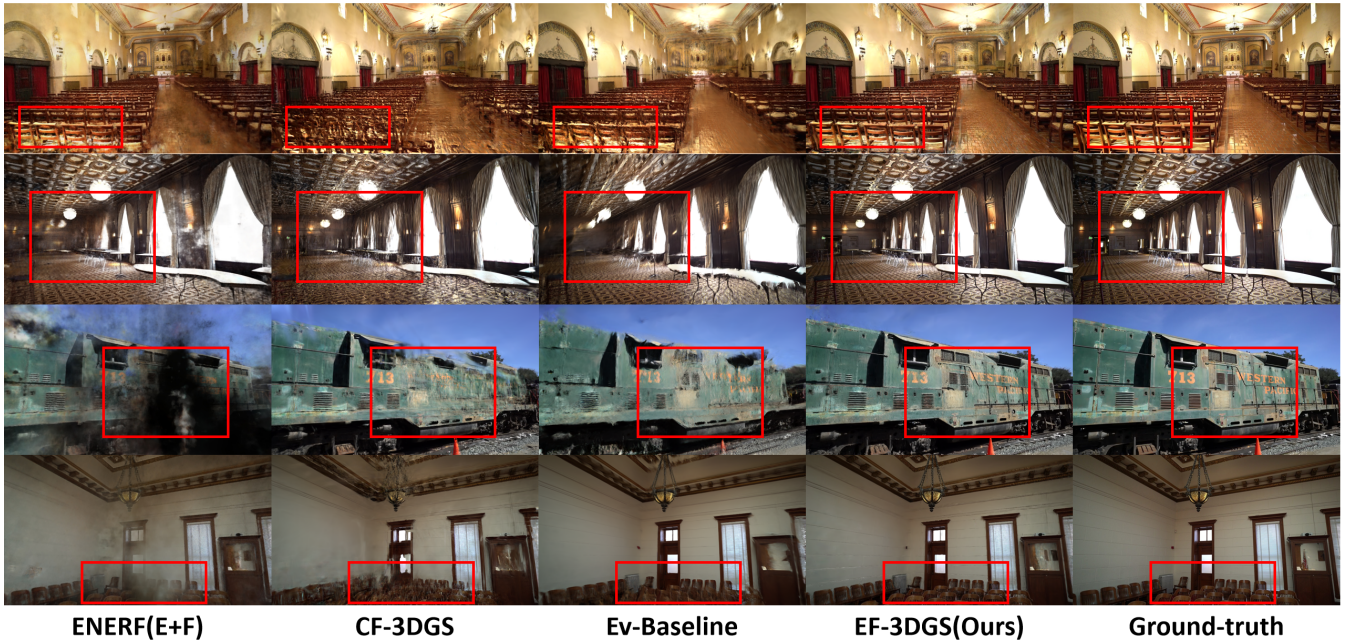| ENERF(E+F) | CF-3DGS | Ev-Baseline | EF-3DGS(Ours) | Ground-truth |

Fig. 4: Qualitative comparison for novel view synthesis on Tanks and Temples. Our approach produces more realistic rendering results with fine-grained details. Better viewed when zoomed in.

set to 0.1, 0.2 and 0.5, respectively, based on subsequent experiment results. For the division of events between adjacent frames, we maintain a constant interval of $\frac{1}{6}$s for Tanks and Temples and $\frac{1}{25}$s for RealEv-DAVIS, setting the number of subinterval N accordingly. For example, in Tanks and Temples, N equals 2 for 3FPS and 6 for 1FPS. This ensures adherence to the constant brightness assumption within each sub-interval and provides adequate events for following CMax warping. The intervals of neighboring warping r in Cmax are set to 3. That is, we warp the three adjacent event frames to the current sampled timestamp.

C. Experimental Setup

1) Metrics: We evaluate all the methods from two aspects: novel view synthesis and pose estimation. For the novel

view synthesis task, we report the standard metrics PSNR, SSIM [59], and LPIPS [60] to quantitatively assess the quality of the rendered images. To measure the accuracy of pose estimation, we adopt the Absolute Trajectory Error (ATE) and Relative Pose Error (RPE) metrics [61], [62], as delineated in [10]. Given that RPE_r and RPE_t measure relative pose errors between adjacent frames, they are inherently influenced by the frame rate. To facilitate a fair comparison across different frame rate settings, we upsample the estimated poses to the same frame rate before evaluation. This enables a consistent comparison of relative pose estimation errors across varying frame rate configurations.

2) Baselines: For a fair comparison, we focus on two categories of methods: those solely based on frames and those leveraging both events and frames. For frame-based
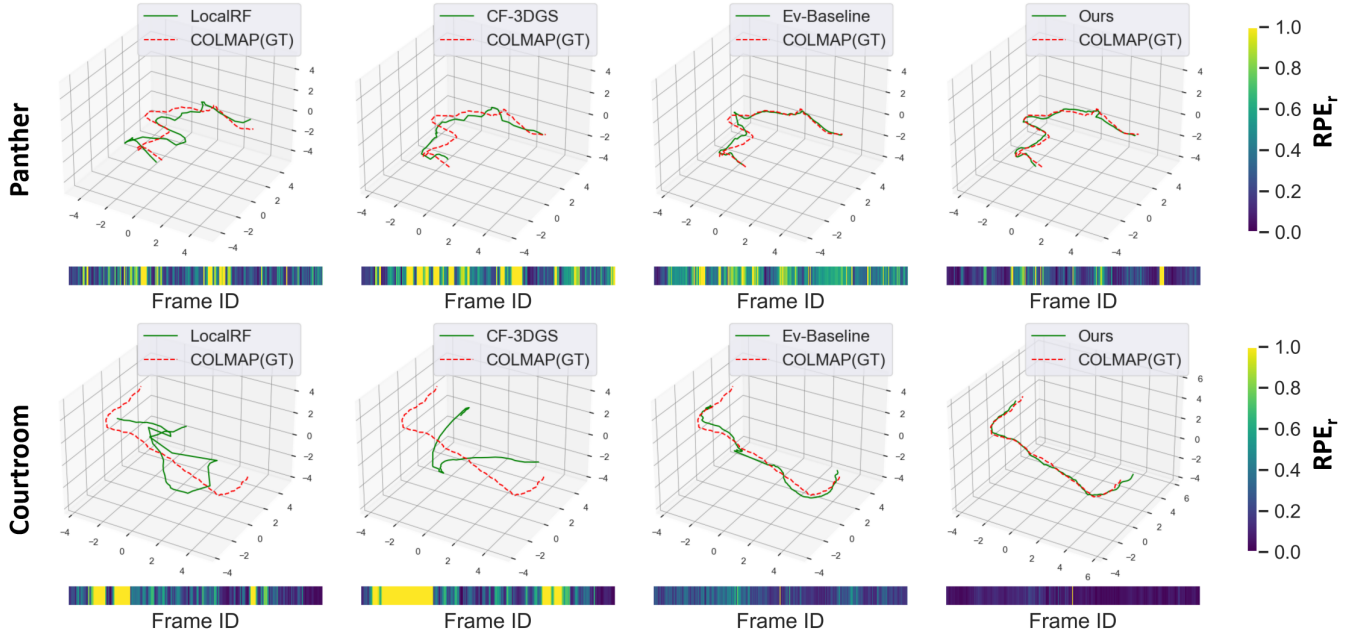
Fig. 5: Pose Estimation Comparison on Tanks and Temples. We visualise the trajectory (3D plot) and RPE_r (color bar) of each method. We clip and normalize the RPE_r by a quarter of the max RPE_r across all results of each scene.

TABLE III: Quantitative Evaluations on RealEv-DAVIS. We select the top-performing methods from the previous evaluation. Each baseline method is trained with its public code under the original settings and evaluated with the same evaluation protocol. The best results are highlighted in bold.

Methods	Pose-Free	Input	SLOW								FAST							
			hall		building		corner		outdoor		hall		building		corner		outdoor	
			PSNR↑	SSIM↑	PSNR↑	SSIM↑	PSNR↑	SSIM↑	PSNR↑	SSIM↑	PSNR↑	SSIM↑	PSNR↑	SSIM↑	PSNR↑	SSIM↑	PSNR↑	SSIM↑
LocalRF	✓	F	18.76	0.5589	20.33	0.5751	21.09	0.5809	23.13	0.7146	17.89	0.4935	16.33	0.4607	17.27	0.4859	19.01	0.6369
CF-3DGS	✓	F	22.37	0.5990	21.33	0.5848	22.48	0.5976	24.52	0.7334	17.33	0.4923	16.92	0.4650	16.67	0.4835	19.42	0.6407
EvDeblurNeRF	×	E+F	20.24	0.5762	19.35	0.5649	20.47	0.5757	22.36	0.7087	18.23	0.5043	16.41	0.4624	17.82	0.4959	19.44	0.6448
ENeRF	×	E+F	21.89	0.5933	21.94	0.5918	22.01	0.5918	23.91	0.7266	20.09	0.5261	18.99	0.4903	19.61	0.5173	20.00	0.6494
Ev-Baseline	✓	E+F	22.58	0.6014	21.71	0.5878	22.61	0.6013	24.66	0.7363	19.01	0.5139	17.99	0.4766	18.81	0.5061	20.70	0.6554
EF-3DGS(Ours)	✓	E+F	**23.43**	**0.6103**	**22.30**	**0.6894**	**23.38**	**0.6210**	**25.50**	**0.7458**	**21.14**	**0.5386**	**20.05**	**0.5016**	**20.68**	**0.5294**	**22.61**	**0.6783**

TABLE IV: Pose accuracy on RealEv-DAVIS. The unit of RPE_r is in degrees, ATE is in the ground truth scale and RPE_t is scaled by 100. Those methods which require precomputed poses are excluded.

Methods	Input	SLOW								FAST							
		hall		building		corner		outdoor		hall		building		corner		outdoor	
		RPE_t↓	RPE_r↓	RPE_t↓	RPE_r↓	RPE_t↓	RPE_r↓	RPE_t↓	RPE_r↓	RPE_t↓	RPE_r↓	RPE_t↓	RPE_r↓	RPE_t↓	RPE_r↓	RPE_t↓	RPE_r↓
LocalRF	F	4.4017	2.5067	4.6186	1.9409	1.9296	2.5183	3.4307	1.3005	5.6061	3.2265	7.0611	2.8722	3.4767	3.8950	4.7229	1.8595
CF-3DGS	F	2.7106	0.6035	3.0374	3.2761	1.9437	1.4954	2.2747	0.8053	3.5025	0.7639	4.6758	4.5256	3.4950	2.2855	3.0551	1.1198
Ev-Baseline	E+F	0.7063	0.4386	3.4225	1.1717	2.1283	**1.3361**	0.8647	**0.3455**	0.8898	0.7734	5.0707	1.6997	3.6785	**2.1552**	1.1645	0.5001
EF-3DGS(Ours)	E+F	**0.5262**	**0.3251**	**2.8008**	**0.4633**	**1.8386**	1.6168	**0.4726**	0.3699	**0.5424**	**0.3464**	**3.5848**	**0.5589**	**2.5396**	2.2157	**0.5218**	**0.4462**

approaches, we selected methods specifically addressing free-trajectory scenarios, such as LocalRF and F2-NeRF, although the latter requires pre-estimated poses. We also include pose-free methods like Nope-NeRF and the current state-of-the-art CF-3DGS. To address the out-of-memory (OOM) issues CF-3DGS faces with long video sequences, we implement a slight modification, segmenting long videos into subsequences for individual reconstruction. For event-based methods, consistent with EvDeblurNeRF [47], we consider approaches that fuse events and frames. This category includes ENeRF [43] and the SOTA deblurring method EvDeblurNeRF [47]. These hybrid approaches leverage the complementary strengths of both data modalities. To the best of our knowledge, no existing method has exploit event cameras to address free-trajectory problem. To facilitate a fair comparison, we construct an event-based baseline method built upon CF-3DGS [5]. It leverages the high temporal resolution property of event cameras by utilizing an event-based frame interpolation network Time Lens [63] to interpolate the original video. Then, the temporally upsampled video frames are subsequently fed into CF-3DGS.

D. Experimental Results

To evaluate the results on synthesized novel views, we select every ten frames as a test image following LocalRF [9]. Since the camera poses are unknown in our setting, we need to estimate the poses of test views. As in NeRFmm [40] and iNeRF [64], we freeze the 3DGS model, initialize the test poses with the poses of the nearest training frames, and optimize the test poses by minimizing the photometric error between rendered images and test views.

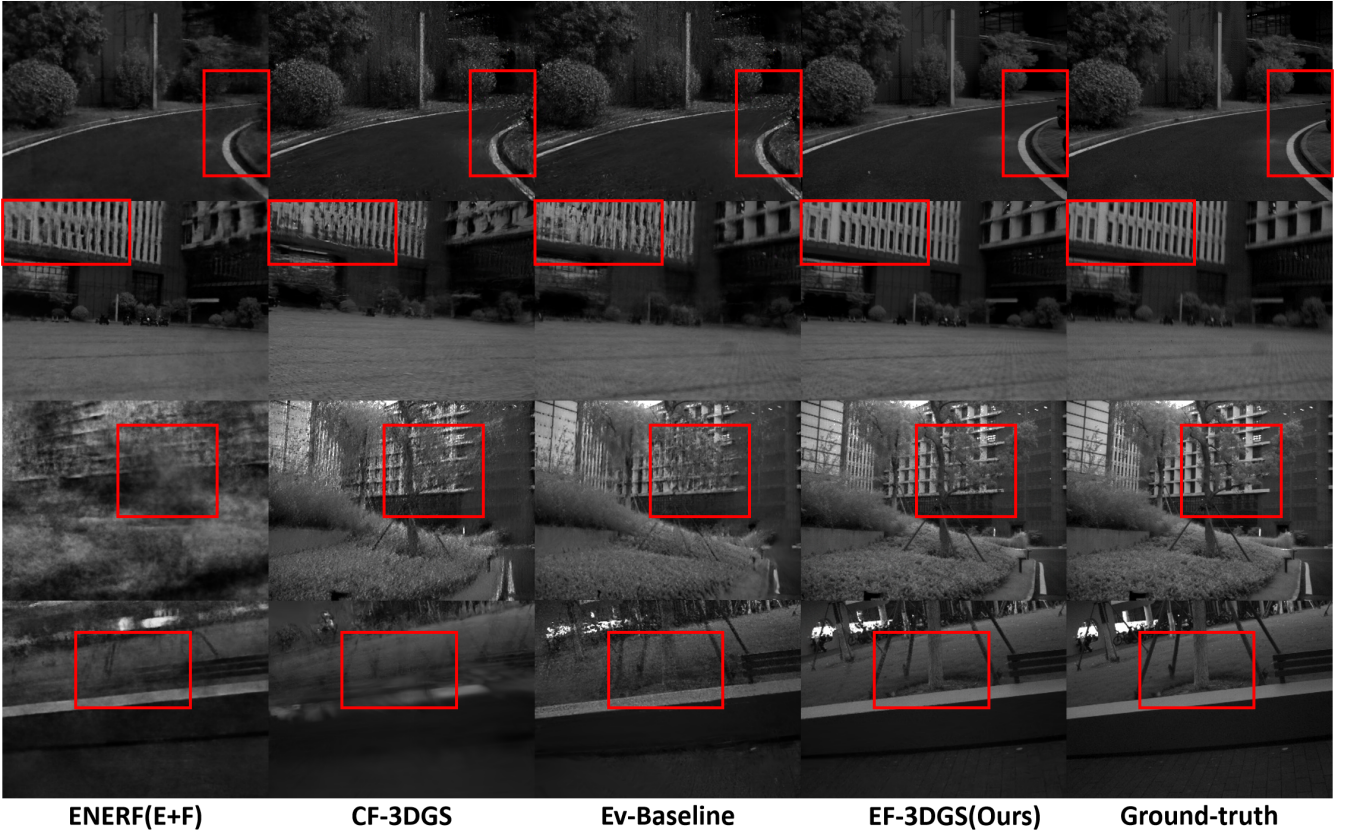| ENERF(E+F) | CF-3DGS | Ev-Baseline | EF-3DGS(Ours) | Ground-truth |

Fig. 6: Qualitative comparison for novel view synthesis on RealEv-DAVIS. Our approach produces more realistic rendering results with fine-grained details. Better viewed when zoomed in.

1) Results on Tanks and Temples: Quantitatively, the experimental results in Table I and Table II demonstrate the superiority of event-based methods (EF-3DGS and Ev-Baseline) over frame-based baselines in both pose estimation accuracy and rendering quality. This highlights the potential of event cameras for free-trajectory scene reconstruction. Furthermore, our method surpasses Ev-Baseline across all evaluation metrics under varying frame rate settings, indicating that our proposed method can better effectively integrate property of the high temporal resolution and motion information encoded in the event streams into the scene reconstruction process.

Qualitatively, as shown in Fig. 4, our method generates more realistic and detailed renderings compared to the baseline. The synthesized views of our method exhibit sharper edges and better preservation of finer textures. In contrast, the baseline methods suffer from various artifacts, such as blurriness and texture inconsistencies. Moreover, the visualization of estimated camera trajectories in Fig. 5 indicates that our estimated trajectory is better aligned with the ground truth than other methods, and the RPE_r is significantly smaller.

2) Results on RealEv-DAVIS: In Table III and Table IV, we report results on the self-collected dataset, RealEv-DAVIS. We select the top-performing methods from the previous evaluation. EF-3DGS demonstrates robust generalization to real-world scenarios, despite challenges such as sensor noise absent in simulated environments. Notably, the performance

gap widens in FAST scenarios, with PSNR improvements of nearly 2 dB over baselines, emphasizing the method's efficacy in handling high-speed motion in real-world settings. Qualitative results in Fig. 6 and Fig. 7 showcase EF-3DGS's superior preservation of fine-grained details and the method's robustness to real-world trajectory.

3) Performance under Varying Camera Speeds: As evidenced in Table I to Table IV, the performance of all methods generally declines as the frame rate decreases. However, our method exhibits remarkable resilience to the reduction in frame rate, maintaining its superiority over the other methods across all metrics. Regarding novel view synthesis quality, the performance gap between the proposed method and the other methods consistently widens as the frame rate decreases. For example, the rendering quality difference between our method and CF-3DGS [5], measured in PSNR, increases from 0.61dB at 6FPS to 3.43dB at 1FPS. This observation demonstrates the robustness of EF-3DGS in handling challenging high-speed scenarios, where the advantages of leveraging event data become more pronounced.

4) Robustness to Pose Disturbance: To further validate the performance of different methods under inaccurate pose initialization, a common challenge in practical scenarios, we introduce varying degrees of perturbations to the initial camera poses estimated by COLMAP. Specifically, following BARF [42], we parametrize the camera poses **p** with the $\mathfrak{se}(3)$ Lie algebra. For each scene, we synthetically perturb
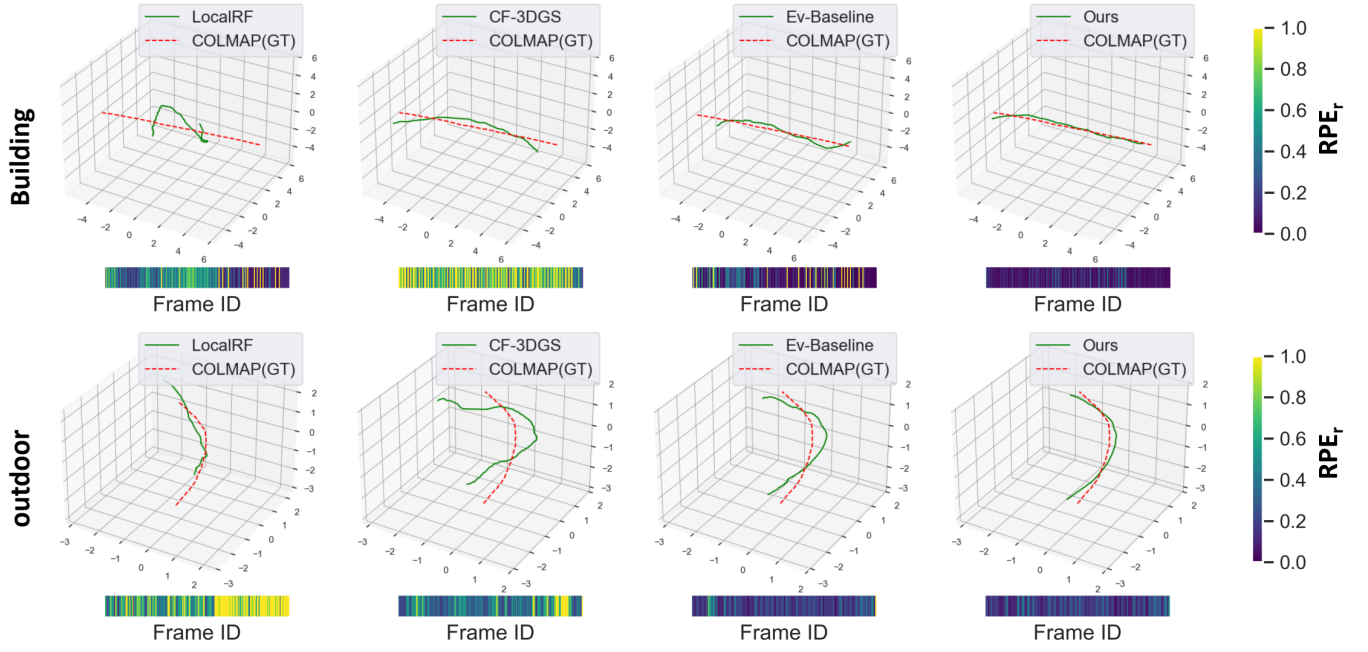
Fig. 7: Pose Estimation Comparison on RealEv-DAVIS. We visualise the trajectory (3D plot) and relative rotation errors RPE_r (color bar) of each method. We clip and normalize the RPE_r by a quarter of the max RPE_r across all results of each scene.
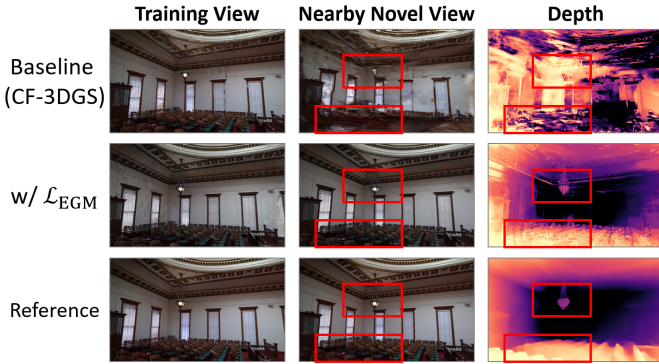

Fig. 8: Qualitative Results of the effectiveness of $\mathcal{L}_{EGM}$.

the camera poses with additive noise $\delta\mathbf{p} \sim \mathcal{N}(\mathbf{0}, n\mathbf{I})$, where n is the noise level. Then, each method is initialized with the noised poses, after which the optimization is performed. The results are illustrated in Fig. 11. Notably, ENeRF [43], which lacks the capability to optimize camera poses, exhibits a drastic performance degradation as the magnitude of pose disturbances increases. This observation validates the critical importance of optimizing camera poses alongside the scene reconstruction. Furthermore, Our proposed framework exhibits superior tolerance across the entire range of pose perturbations compared to existing methods. Even in the presence of significant perturbation, the degradation in EF-3DGS's novel view synthesis fidelity and trajectory estimation performance is substantially lower than that of the other methods.

E. Ablation Studies

To further investigate the effectiveness of each key component in our proposed EF-3DGS framework, we conduct

TABLE V: **Effect of each component in EF-3DGS.** Evaluation is conducted on 1FPS scenes of Tanks and Temples. The best results are highlighted in bold.

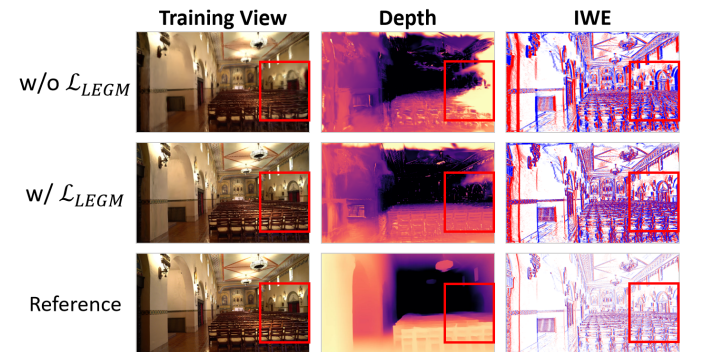| $\mathcal{L}_{EGM}$	$\mathcal{L}_{LEGM}$	$\mathcal{L}_{PBA}$	Fixed GS	NVS			Pose		
				PSNR↑	SSIM↑	LPIPS↓	RPE_t↓	RPE_r↓	ATE↓
				20.53	0.65	0.46	0.1057	0.9768	0.8972
✓				22.16	0.68	0.42	0.0651	0.7529	0.5779
	✓			21.07	0.67	0.44	0.0830	0.8869	0.7231
		✓		20.96	0.65	0.46	0.0938	0.9875	0.9112
✓	✓			22.83	0.68	0.40	0.0523	0.6387	0.3981
✓	✓		✓	23.46	0.70	0.37	0.0523	0.6387	0.3981
✓	✓	✓		23.09	0.70	0.38	**0.0487**	**0.6259**	**0.3753**
✓	✓	✓	✓	**23.96**	**0.72**	**0.36**	**0.0487**	**0.6259**	**0.3753**

Fig. 9: Qualitative Results of the effectiveness of $\mathcal{L}_{LEGM}$.

ablation experiments under the 1 FPS setting on the Tanks and Temples dataset. The results are presented in Table V.

1) Effect of $\mathcal{L}_{EGM}$: Analysis of Table V demonstrates that removing all components substantially degrades both rendering quality and pose estimation accuracy. This finding underscores the significant challenges faced by the original CF-3DGS in high-speed scenarios. Fig. 8 further illustrates this issue, revealing that while CF-3DGS can produce high-quality
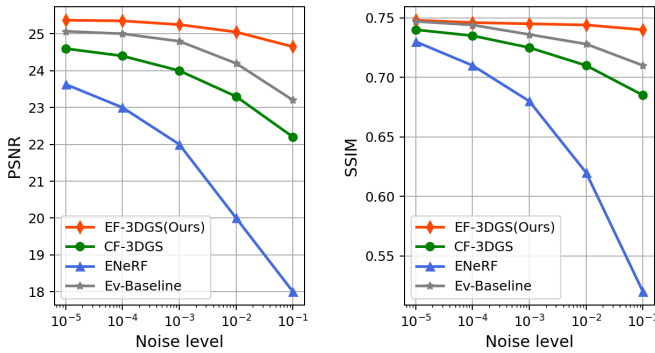
w/o $\mathcal{L}_{PBA}$, w/o *Fixed GS*   w/ $\mathcal{L}_{PBA}$, w/o *Fixed GS*

w/ $\mathcal{L}_{PBA}$, w/ *Fixed GS*   Gound truth

Fig. 10: Qualitative Results of the effectiveness of $\mathcal{L}_{PBA}$.

Fig. 11: Robustness of different methods to pose disturbance.

TABLE VI: Effect of the number of event subintervals N.

	PSNR↑	FPS↑	t↓
$N = 2$	23.56	30+	1.3h
$N = 3$	24.43	30+	3h
$N = 6$	**24.81**	30+	7h
LocalRF	21.20	<1	8h
CF-3DGS	22.08	30+	3h

Fig. 12: Comparison of training time vs PSNR for various methods

renderings at training views, it struggles with adjacent novel views. Moreover, the rendered depth maps expose considerable inaccuracies in CF-3DGS's scene geometry reconstruction. The incorporation of $\mathcal{L}_{\mathbf{EGM}}$ yields marked improvements in both rendering quality and pose estimation precision, as evidenced by Table V and Fig. 8. This experimental outcome suggests that $\mathcal{L}_{\mathbf{EGM}}$ effectively harnesses the continuous brightness change data captured by event cameras, thereby compensating for the inter-frame loss of scene brightness information. Consequently, the 3DGS training optimization achieves multi-view geometric consistency. Notably, among all components, $\mathcal{L}_{\mathbf{EGM}}$ demonstrates the most profound impact on overall method performance, establishing its role as a fundamental component of our approach.

2) Effect of $\mathcal{L}_{LEGM}$: As demonstrated in Table V, $\mathcal{L}_{LEGM}$ further enhances both rendering quality and pose estimation accuracy when applied in conjunction with $\mathcal{L}_{\mathbf{EGM}}$. Fig. 9 provides a visual illustration of $\mathcal{L}_{LEGM}$'s efficacy. Ideally, with accurate depth and pose estimation, the Image of Warped Events (IWE) should resemble the reference image. However, in the absence of $\mathcal{L}_{LEGM}$, the generated IWE exhibits blurring effects, indicative of inaccurate pose estimation. More critically, as highlighted in the boxed area of Fig. 9, the presence of self-similar regions with repetitive textures poses additional challenges for scene reconstuction and pose estimation. Significant errors in scene reconstruction leading to inaccurate depth estimates further compromise the inherent

structure of the IWE. The introduction of $\mathcal{L}_{\mathbf{LEGM}}$ allows for the simultaneous reflection of both pose estimation and scene reconstruction errors in the IWE. By optimizing the sharpness of the IWE, $\mathcal{L}_{\mathbf{LEGM}}$ effectively improves both rendering quality and pose estimation precision.

3) Effect of $\mathcal{L}_{PBA}$ and Fixed-GS Strategy: Comparing the last three rows of Table V, we observe that both $\mathcal{L}_{\mathbf{PBA}}$ and Fixed-GS strategies significantly enhance rendering quality. $\mathcal{L}_{\mathbf{PBA}}$, by enforcing multi-view consistency, slightly improves pose estimation accuracy, while the Fixed-GS strategy, applied solely during scene optimization, has no impact on pose estimation. Fig. 10 visualizes the effects of these components. When both are removed, the reconstructed scene loses almost all color information. This is attributed to the substantially higher number of event frames than image frames, causing event-guided optimization to dominate scene reconstruction and suppress color information from image frames. $\mathcal{L}_{\mathbf{PBA}}$ alone, which reprojects neighboring video frames onto event frames, only partially mitigates this imbalance. The Fixed-GS strategy employs a two-stage scene optimization approach for the separation of the color and structure of the scene. However, this approach does not fully leverage the supervisory signals from adjacent frames. The combination of $\mathcal{L}_{\mathbf{PBA}}$ and Fixed-GS strategies complements each other, more effectively addressing the color distortion issue.

4) Computational Efficiency and Impact of Subinterval Number N: To investigate the impact of the number of subintervals N on our method, we conduct ablation studies on the Tanks and Temples dataset under the 2 FPS setting. The results are shown in Table VI and figure on the right. We test the speed on RTX2080ti. Note that in the t-PSNR figure, circular nodes represent pose-free methods, while diamond-shaped nodes indicate methods that require precomputed poses. The results in Table VI reveal that increasing N improves PSNR, indicating that finer temporal discretization enhances reconstruction quality. However, this improvement comes at the cost of extended training time, increasing from 1.3 hours at N=2 to 7 hours at N=6. Notably, our method maintains real-time rendering performance, thanks to the efficient rendering capabilities of 3DGS. Even at N=2, our approach outperforms baselines in both PSNR and rendering speed. The setting of N=3 offers a good balance, achieving higher PSNR than CF-3DGS with comparable training time. However, it's important
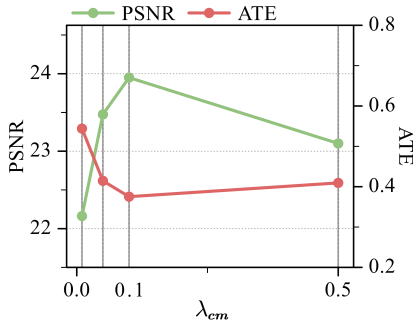
Fig. 13: Study of the different evaluation metrics with respect to λ_{cm}
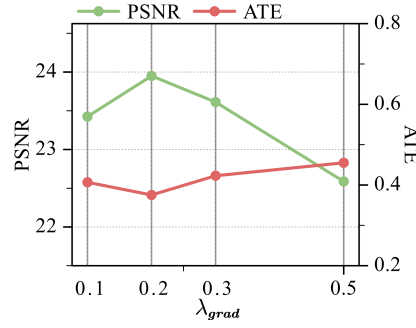

Fig. 14: Study of the different evaluation metrics with respect to λ_{grad}
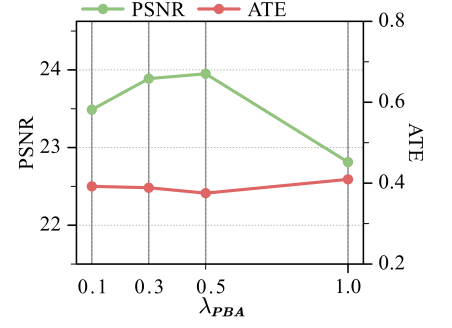

Fig. 15: Study of the different evaluation metrics with respect to λ_{PBA}

to note that the optimal N may vary for different frame rates and motion characteristics.

F. Analysis of Loss Coefficients

Different components of our method play crucial roles in overall performance. To comprehensively understand these effects and determine optimal weight settings, we conducted a detailed analysis of the loss weights: λ_{cm}, λ_{grad} and λ_{PBA}.

1) Contrast Maximization Coefficient λ_{cm}: As shown in Fig. 13, the contrast maximization coefficient λ_{cm} significantly affects both NVS quality and pose estimation. We observe that a value of 0.1 achieves the best overall performance. Lower values (0.01) lead to decreased performance, likely due to insufficient utilization of motion information from events. Higher values (0.5) also result in performance degradation, possibly due to over-reliance on the contrast maximization term at the expense of other constraints. The optimal λ_{cm} suggests that while event data is crucial, it should not dominate the reconstruction process. This balance allows our method to leverage the high temporal resolution of events without sacrificing the global supervision provided by frame data.

2) Gradient-based Loss Coefficient λ_{grad}: As shown in Fig. 14, the gradient-based loss coefficient λ_{grad} shows optimal performance at 0.2. Lower values (0.1) slightly decrease performance, while higher values (0.3, 0.5) lead to more significant drops in both NVS quality and pose accuracy. This is likely because $\mathcal{L}_{EGM}$ and 3DGS primarily focus on rendering absolute brightness, and excessive gradient constraints may interfere with this process. Therefore, a moderate λ_{grad} value is crucial to balance gradient information with the primary rendering objectives.

3) Photometric Bundle Adjustment Coefficient λ_{PBA}: As illustrated in Figure 15, our method demonstrates remarkable stability across λ_{PBA} values ranging from 0.1 to 0.5. However, Fig. 10 illustrates that while $\mathcal{L}_{PBA}$ has minimal effect on PSNR and ATE metrics, its absence leads to noticeable color distortion artifacts in visual results. This underscores the importance of λ_{PBA} in maintaining visual fidelity. Conversely, setting λ_{PBA} to 1.0 results in significant performance degradation, indicating that overemphasis on cross-view consistency can be counterproductive.

VI. LIMITATIONS

Our method combines event streams with conventional video frames, which require the input data to be time-ordered. So it can not handle the unordered image input. In high-speed situations, video frames may suffer from severe motion blur, which can degrade the quality of the visual information. Future research could focus on this challenge. And, our method relies on several key parameters (e.g., λ_{cm}, λ_{grad} and λ_{PBA}) that may require manual tuning for optimal performance across different speed scenarios. This dependency on scene-specific parameter settings could limit the method's adaptability to diverse environments. Future work should explore self-adaptive parameter adjustment strategies to enhance the method's versatility and ease of use across various reconstruction tasks.

VII. CONCLUSIONS

In this work, we propose Event-Aided Free-Trajectory 3DGS (EF-3DGS), a novel framework that seamlessly integrates event camera data into the task of reconstructing 3DGS from casually captured free-trajectory videos. Our method effectively leverages the high temporal resolution and motion information encoded in event streams to enhance the 3DGS optimization process, leading to improved rendering quality and accurate camera pose estimation.

REFERENCES

[1] B. Mildenhall, P. P. Srinivasan, M. Tancik, J. T. Barron, R. Ramamoorthi, and R. Ng, "Nerf: Representing scenes as neural radiance fields for view synthesis," in *ECCV*, 2020.

[2] J. T. Barron, B. Mildenhall, D. Verbin, P. P. Srinivasan, and P. Hedman, "Mip-nerf 360: Unbounded anti-aliased neural radiance fields," in *Proceedings of the IEEE/CVF Conference on Computer Vision and Pattern Recognition (CVPR)*, June 2022, pp. 5470–5479.

[3] T. Müller, A. Evans, C. Schied, and A. Keller, "Instant neural graphics primitives with a multiresolution hash encoding," *ACM Trans. Graph.*, vol. 41, no. 4, jul 2022. [Online]. Available: https://doi.org/10.1145/3528223.3530127

[4] B. Kerbl, G. Kopanas, T. Leimkühler, and G. Drettakis, "3d gaussian splatting for real-time radiance field rendering," *ACM Transactions on Graphics*, vol. 42, no. 4, July 2023. [Online]. Available: https://repo-sam.inria.fr/fungraph/3d-gaussian-splatting/

[5] Y. Fu, S. Liu, A. Kulkarni, J. Kautz, A. A. Efros, and X. Wang, "Colmap-free 3d gaussian splatting," 2024. [Online]. Available: https://arxiv.org/abs/2312.07504

[6] A. Chen, Z. Xu, A. Geiger, J. Yu, and H. Su, "Tensorf: Tensorial radiance fields," in *Computer Vision – ECCV 2022*, S. Avidan, G. Brostow, M. Cissé, G. M. Farinella, and T. Hassner, Eds. Cham: Springer Nature Switzerland, 2022, pp. 333–350.

[7] J. T. Barron, B. Mildenhall, D. Verbin, P. P. Srinivasan, and P. Hedman, "Zip-nerf: Anti-aliased grid-based neural radiance fields," in *Proceedings of the IEEE/CVF International Conference on Computer Vision (ICCV)*, October 2023, pp. 19 697–19 705.

[8] P. Wang, Y. Liu, Z. Chen, L. Liu, Z. Liu, T. Komura, C. Theobalt, and W. Wang, "F2-nerf: Fast neural radiance field training with free camera trajectories," in *Proceedings of the IEEE/CVF Conference on Computer Vision and Pattern Recognition (CVPR)*, June 2023, pp. 4150–4159.

[9] A. Meuleman, Y.-L. Liu, C. Gao, J.-B. Huang, C. Kim, M. H. Kim, and J. Kopf, "Progressively optimized local radiance fields for robust view synthesis," in *Proceedings of the IEEE/CVF Conference on Computer Vision and Pattern Recognition (CVPR)*, June 2023, pp. 16 539–16 548.

[10] W. Bian, Z. Wang, K. Li, J.-W. Bian, and V. A. Prisacariu, "Nope-nerf: Optimising neural radiance field with no pose prior," in *Proceedings of the IEEE/CVF Conference on Computer Vision and Pattern Recognition (CVPR)*, June 2023, pp. 4160–4169.

[11] S. M. H. Miangoleh, S. Dille, L. Mai, S. Paris, and Y. Aksoy, "Boosting monocular depth estimation models to high-resolution via content-adaptive multi-resolution merging," in *Proceedings of the IEEE/CVF Conference on Computer Vision and Pattern Recognition (CVPR)*, June 2021, pp. 9685–9694.

[12] R. Ranftl, A. Bochkovskiy, and V. Koltun, "Vision transformers for dense prediction," in *Proceedings of the IEEE/CVF International Conference on Computer Vision (ICCV)*, October 2021, pp. 12 179–12 188.

[13] R. Ranftl, K. Lasinger, D. Hafner, K. Schindler, and V. Koltun, "Towards robust monocular depth estimation: Mixing datasets for zero-shot cross-dataset transfer," *IEEE Transactions on Pattern Analysis and Machine Intelligence*, vol. 44, no. 3, pp. 1623–1637, 2022.

[14] Z. Teed and J. Deng, "Raft: Recurrent all-pairs field transforms for optical flow," in *Computer Vision – ECCV 2020*, A. Vedaldi, H. Bischof, T. Brox, and J.-M. Frahm, Eds. Cham: Springer International Publishing, 2020, pp. 402–419.

[15] M. Niemeyer, J. T. Barron, B. Mildenhall, M. S. M. Sajjadi, A. Geiger, and N. Radwan, "Regnerf: Regularizing neural radiance fields for view synthesis from sparse inputs," in *Proceedings of the IEEE/CVF Conference on Computer Vision and Pattern Recognition (CVPR)*, June 2022, pp. 5480–5490.

[16] G. Wang, Z. Chen, C. C. Loy, and Z. Liu, "Sparsenerf: Distilling depth ranking for few-shot novel view synthesis," in *Proceedings of the IEEE/CVF International Conference on Computer Vision (ICCV)*, October 2023, pp. 9065–9076.

[17] P. Truong, M.-J. Rakotosaona, F. Manhardt, and F. Tombari, "Sparf: Neural radiance fields from sparse and noisy poses," in *Proceedings of the IEEE/CVF Conference on Computer Vision and Pattern Recognition (CVPR)*, June 2023, pp. 4190–4200.

[18] G. Gallego, T. Delbrück, G. Orchard, C. Bartolozzi, B. Taba, A. Censi, S. Leutenegger, A. J. Davison, J. Conradt, K. Daniilidis, and D. Scaramuzza, "Event-based vision: A survey," *IEEE Transactions on Pattern Analysis and Machine Intelligence*, vol. 44, no. 1, pp. 154–180, 2022.

[19] J. Hidalgo-Carrió, G. Gallego, and D. Scaramuzza, "Event-aided direct sparse odometry," in *Proceedings of the IEEE/CVF Conference on Computer Vision and Pattern Recognition (CVPR)*, June 2022, pp. 5781–5790.

[20] A. R. Vidal, H. Rebecq, T. Horstschaefer, and D. Scaramuzza, "Ultimate slam? combining events, images, and imu for robust visual slam in hdr and high-speed scenarios," *IEEE Robotics and Automation Letters*, vol. 3, no. 2, pp. 994–1001, 2018.

[21] Z. Wan, Y. Wang, Z. Wei, G. Tan, Y. Cao, and Z.-J. Zha, "Event-based optical flow via transforming into motion-dependent view," *IEEE Transactions on Image Processing*, 2024.

[22] Y. Wu, G. Tan, J. Chen, W. Zhai, Y. Cao, and Z.-J. Zha, "Event-based asynchronous hdr imaging by temporal incident light modulation," *Optics Express*, vol. 32, no. 11, pp. 18 527–18 538, 2024.

[23] C. Cao, X. Fu, Y. Zhu, Z. Sun, and Z.-J. Zha, "Event-driven video restoration with spiking-convolutional architecture," *IEEE Transactions on Neural Networks and Learning Systems*, pp. 1–15, 2023.

[24] D. Liu, A. Parra, and T.-J. Chin, "Globally optimal contrast maximisation for event-based motion estimation," in *Proceedings of the IEEE/CVF Conference on Computer Vision and Pattern Recognition (CVPR)*, June 2020.

[25] G. Tan, Z. Wan, Y. Wang, Y. Cao, and Z.-J. Zha, "Tackling event-based lip-reading by exploring multigrained spatiotemporal clues," *IEEE Transactions on Neural Networks and Learning Systems*, pp. 1–13, 2024.

[26] A. Ussa, C. S. Rajen, T. Pulluri, D. Singla, J. Acharya, G. F. Chuanrong, A. Basu, and B. Ramesh, "A hybrid neuromorphic object tracking and classification framework for real-time systems," *IEEE Transactions on*

[27] L. A. Camuñas-Mesa, T. Serrano-Gotarredona, S.-H. Ieng, R. Benosman, and B. Linares-Barranco, "Event-driven stereo visual tracking algorithm to solve object occlusion," *IEEE Transactions on Neural Networks and Learning Systems*, vol. 29, no. 9, pp. 4223–4237, 2018.

[28] G. Gallego, H. Rebecq, and D. Scaramuzza, "A unifying contrast maximization framework for event cameras, with applications to motion, depth, and optical flow estimation," in *Proceedings of the IEEE Conference on Computer Vision and Pattern Recognition (CVPR)*, June 2018.

[29] G. Gallego, C. Forster, E. Mueggler, and D. Scaramuzza, "Event-based camera pose tracking using a generative event model," 2015.

[30] D. Gehrig, H. Rebecq, G. Gallego, and D. Scaramuzza, "Asynchronous, photometric feature tracking using events and frames," in *Proceedings of the European Conference on Computer Vision (ECCV)*, September 2018.

[31] S. Agarwal, Y. Furukawa, N. Snavely, I. Simon, B. Curless, S. M. Seitz, and R. Szeliski, "Building rome in a day," *Communications of the ACM*, vol. 54, no. 10, pp. 105–112, 2011.

[32] N. Snavely, S. M. Seitz, and R. Szeliski, "Photo tourism: exploring photo collections in 3d," in *ACM siggraph 2006 papers*, 2006, pp. 835–846.

[33] K. Zhang, G. Riegler, N. Snavely, and V. Koltun, "Nerf++: Analyzing and improving neural radiance fields," 2020.

[34] T. Neff, P. Stadlbauer, M. Parger, A. Kurz, J. H. Mueller, C. R. A. Chaitanya, A. Kaplanyan, and M. Steinberger, "Donerf: Towards real-time rendering of compact neural radiance fields using depth oracle networks," *Computer Graphics Forum*, vol. 40, no. 4, pp. 45–59, 2021. [Online]. Available: https://onlinelibrary.wiley.com/doi/abs/10.1111/cgf.14340

[35] H. Turki, D. Ramanan, and M. Satyanarayanan, "Mega-nerf: Scalable construction of large-scale nerfs for virtual fly-throughs," in *Proceedings of the IEEE/CVF Conference on Computer Vision and Pattern Recognition (CVPR)*, June 2022, pp. 12 922–12 931.

[36] M. Tancik, V. Casser, X. Yan, S. Pradhan, B. Mildenhall, P. P. Srinivasan, J. T. Barron, and H. Kretzschmar, "Block-nerf: Scalable large scene neural view synthesis," in *Proceedings of the IEEE/CVF Conference on Computer Vision and Pattern Recognition (CVPR)*, June 2022, pp. 8248–8258.

[37] Y. Liu, H. Guan, C. Luo, L. Fan, J. Peng, and Z. Zhang, "Citygaussian: Real-time high-quality large-scale scene rendering with gaussians," *arXiv preprint arXiv:2404.01133*, 2024.

[38] J. Lin, Z. Li, X. Tang, J. Liu, S. Liu, J. Liu, Y. Lu, X. Wu, S. Xu, Y. Yan et al., "Vastgaussian: Vast 3d gaussians for large scene reconstruction," in *Proceedings of the IEEE/CVF Conference on Computer Vision and Pattern Recognition*, 2024, pp. 5166–5175.

[39] J. L. Schonberger and J.-M. Frahm, "Structure-from-motion revisited," in *Proceedings of the IEEE Conference on Computer Vision and Pattern Recognition (CVPR)*, June 2016.

[40] Z. Wang, S. Wu, W. Xie, M. Chen, and V. A. Prisacariu, "Nerf–: Neural radiance fields without known camera parameters," 2022.

[41] S.-F. Chng, S. Ramasinghe, J. Sherrah, and S. Lucey, "Gaussian activated neural radiance fields for high fidelity reconstruction and pose estimation," in *Computer Vision – ECCV 2022*, S. Avidan, G. Brostow, M. Cissé, G. M. Farinella, and T. Hassner, Eds. Cham: Springer Nature Switzerland, 2022, pp. 264–280.

[42] C.-H. Lin, W.-C. Ma, A. Torralba, and S. Lucey, "Barf: Bundle-adjusting neural radiance fields," in *Proceedings of the IEEE/CVF International Conference on Computer Vision (ICCV)*, October 2021, pp. 5741–5751.

[43] S. Klenk, L. Koestler, D. Scaramuzza, and D. Cremers, "E-nerf: Neural radiance fields from a moving event camera," *IEEE Robotics and Automation Letters*, vol. 8, no. 3, pp. 1587–1594, 2023.

[44] V. Rudnev, M. Elgharib, C. Theobalt, and V. Golyanik, "Eventnerf: Neural radiance fields from a single colour event camera," in *Proceedings of the IEEE/CVF Conference on Computer Vision and Pattern Recognition (CVPR)*, June 2023, pp. 4992–5002.

[45] W. F. Low and G. H. Lee, "Robust e-nerf: Nerf from sparse & noisy events under non-uniform motion," in *Proceedings of the IEEE/CVF International Conference on Computer Vision (ICCV)*, October 2023, pp. 18 335–18 346.

[46] Y. Qi, L. Zhu, Y. Zhang, and J. Li, "E2nerf: Event enhanced neural radiance fields from blurry images," in *Proceedings of the IEEE/CVF International Conference on Computer Vision (ICCV)*, October 2023, pp. 13 254–13 264.

[47] M. Cannici and D. Scaramuzza, "Mitigating motion blur in neural radiance fields with events and frames," in *Proceedings of the IEEE/CVF*

Conference on Computer Vision and Pattern Recognition, 2024, pp. 9286–9296.

[48] L. Pan, C. Scheerlinck, X. Yu, R. Hartley, M. Liu, and Y. Dai, "Bringing a blurry frame alive at high frame-rate with an event camera," in *Proceedings of the IEEE/CVF Conference on Computer Vision and Pattern Recognition (CVPR)*, June 2019.

[49] Q. Ma, D. P. Paudel, A. Chhatkuli, and L. Van Gool, "Deformable neural radiance fields using rgb and event cameras," in *Proceedings of the IEEE/CVF International Conference on Computer Vision (ICCV)*, October 2023, pp. 3590–3600.

[50] A. Bhattacharya, R. Madaan, F. Cladera, S. Vemprala, R. Bonatti, K. Daniilidis, A. Kapoor, V. Kumar, N. Matni, and J. K. Gupta, "Evd-nerf: Reconstructing event data with dynamic neural radiance fields," in *Proceedings of the IEEE/CVF Winter Conference on Applications of Computer Vision (WACV)*, January 2024, pp. 5846–5855.

[51] X. Peng, L. Gao, Y. Wang, and L. Kneip, "Globally-optimal contrast maximisation for event cameras," *IEEE Transactions on Pattern Analysis and Machine Intelligence*, vol. 44, no. 7, pp. 3479–3495, 2022.

[52] T. Stoffregen and L. Kleeman, "Event cameras, contrast maximization and reward functions: An analysis," in *Proceedings of the IEEE/CVF Conference on Computer Vision and Pattern Recognition (CVPR)*, June 2019.

[53] Z. Zhang, A. Yezzi, and G. Gallego, "Formulating event-based image reconstruction as a linear inverse problem with deep regularization using optical flow," *IEEE Transactions on Pattern Analysis and Machine Intelligence*, p. 1–18, 2022. [Online]. Available: http://dx.doi.org/10.1109/TPAMI.2022.3230727

[54] L. Shen, J. Pauly, and L. Xing, "Nerp: Implicit neural representation learning with prior embedding for sparsely sampled image reconstruction," *IEEE Transactions on Neural Networks and Learning Systems*, vol. 35, no. 1, pp. 770–782, 2024.

[55] A. Knapitsch, J. Park, Q.-Y. Zhou, and V. Koltun, "Tanks and temples: benchmarking large-scale scene reconstruction," *ACM Trans. Graph.*, vol. 36, no. 4, jul 2017. [Online]. Available: https://doi.org/10.1145/3072959.3073599

[56] Z. Huang, T. Zhang, W. Heng, B. Shi, and S. Zhou, "Real-time intermediate flow estimation for video frame interpolation," in *Computer Vision – ECCV 2022*, S. Avidan, G. Brostow, M. Cissé, G. M. Farinella, and T. Hassner, Eds. Cham: Springer Nature Switzerland, 2022, pp. 624–642.

[57] D. Gehrig, M. Gehrig, J. Hidalgo-Carrió, and D. Scaramuzza, "Video to events: Recycling video datasets for event cameras," in *IEEE Conf. Comput. Vis. Pattern Recog. (CVPR)*, June 2020.

[58] D. P. Kingma and J. Ba, "Adam: A method for stochastic optimization," 2017.

[59] Z. Wang, A. Bovik, H. Sheikh, and E. Simoncelli, "Image quality assessment: from error visibility to structural similarity," *IEEE Transactions on Image Processing*, vol. 13, no. 4, pp. 600–612, 2004.

[60] R. Zhang, P. Isola, A. A. Efros, E. Shechtman, and O. Wang, "The unreasonable effectiveness of deep features as a perceptual metric," in *Proceedings of the IEEE Conference on Computer Vision and Pattern Recognition (CVPR)*, June 2018.

[61] Z. Zhang and D. Scaramuzza, "A tutorial on quantitative trajectory evaluation for visual(-inertial) odometry," in *2018 IEEE/RSJ International Conference on Intelligent Robots and Systems (IROS)*, 2018, pp. 7244–7251.

[62] J. Sturm, N. Engelhard, F. Endres, W. Burgard, and D. Cremers, "A benchmark for the evaluation of rgb-d slam systems," in *2012 IEEE/RSJ International Conference on Intelligent Robots and Systems*, 2012, pp. 573–580.

[63] S. Tulyakov, D. Gehrig, S. Georgoulis, J. Erbach, M. Gehrig, Y. Li, and D. Scaramuzza, "Time lens: Event-based video frame interpolation," in *Proceedings of the IEEE/CVF Conference on Computer Vision and Pattern Recognition (CVPR)*, June 2021, pp. 16 155–16 164.

[64] L. Yen-Chen, P. Florence, J. T. Barron, A. Rodriguez, P. Isola, and T.-Y. Lin, "inerf: Inverting neural radiance fields for pose estimation," in *2021 IEEE/RSJ International Conference on Intelligent Robots and Systems (IROS)*, 2021, pp. 1323–1330.